Int. J. Electrochem. Sci., 7 **(2012)** 10865 - 10883

International Journal of
ELECTROCHEMICAL
SCIENCE
www.electrochemsci.org

Tunable Ordered Nanostructured α-Fe_2O_3 Lithium Battery Anodes by Nanocasting Technique Using SBA-15 Hard Silica Templates

F. Di Lupo[1,*], *A. Tuel*[2], *C. Francia*[1], *G. Meligrana*[1], *S. Bodoardo*[1], *C. Gerbaldi*[1,*]

[1] Institute of Chemistry, Department of Applied Science and Technology (DISAT), Politecnico di Torino, C.so Duca degli Abruzzi 24, 10129 Torino (ITALY)
[2] IRCELYON, Institut de Recherches sur la Catalyse et l'environnement de Lyon, UMR 5256, CNRS-Université de Lyon 1, 2 Avenue Albert Einstein, 69626 Villeurbanne Cedex (FRANCE)
[*]E-mail: claudio.gerbaldi@polito.it; francesca.dilupo@polito.it

Received: 10 September 2012 / *Accepted:* 28 September 2012 / *Published:* 1 November 2012

Nanostructured α-Fe_2O_3 have been obtained through a nanocasting strategy using different SBA-15 mesoporous silicas as hard templates. In order to tune the micro/mesoporous structure of the resulting α-Fe_2O_3 nanostructures, SBA-15 silica templates with different textural features were prepared by varying the temperature at which their synthesis was carried out. X-Ray powder diffraction, transmission electron microscopy and N_2 physisorption at 77 K techniques were employed for the structural-morphological characterization of the synthesized materials. Cyclic voltammetry and galvanostatic discharge/charge cycling tests were carried out to assess the electrochemical behaviour of the nanostructured α-Fe_2O_3 as a promising anode material for Li-ion cells. This work demonstrated that the structural-morphological features change accordingly to the different templates used and a careful control of the texture/particle characteristics is likely a fundamental variable which noticeably affects the cycling behaviour of the samples.

Keywords: nanostructured iron oxide; SBA-15 silica; nanocasting technique; anode material; electrochemical characterization; lithium battery

1. INTRODUCTION

In traditional intercalation materials the transfer of lithium ions is inherently limited so that the electrochemical capacity is more often lower than the theoretical values. It is not surprising, therefore, that extensive research is actually devoted at improving these intrinsic limitations [1,2]. Ordinary graphite anodes are able to efficiently intercalate lithium but present specific capacity limitations, particularly at elevated current regimes [3]. Nevertheless, at the beginning of 21st century, an important discovery in the field of anode materials showed the way to a new reactivity concept: the reversible electrochemical reaction of lithium with a range of transition-metal oxides by a process termed conversion [2,4].

During the investigation of transition metal oxides (TMO) reactivity, a particular Li electrochemical activity was pointed out. According to Poizot et al. [5], oxides, typically Co, Fe, Ni, Cu and Mn, do not react with lithium through the classical processes of Li insertion/deinsertion or Li alloying: in fact, such oxides can store Li reversibly, upon complete reduction of the metal, according to the following simplified equation [4,6]:

$$Li^+ + TMO + e^- \rightarrow Li_2O + TM \qquad (1)$$

During the first discharge (TM reduction), the mechanism of Li reactivity is due to the *in situ* formation of metal nanoparticles, which allows to obtain a Li_2O-matrix [4]. When a reverse polarization is applied (charge, TM oxidation), the opposite reaction can occur reversibly and, due to the large extent of the surface area, the very inert Li_2O solid can react with the transition metal at room temperature [6], leading to the decomposition of the Li_2O-matrix [7]. The ability of iron oxide to act as a conversion material is known since the ‘80s and the high theoretical capacity values related to its conversion (i.e., above 1000 mAh g^{-1}), in addition to its availability, non-toxicity and low cost, make this material suitable for large-scale lithium battery applications [7]. One of the disadvantages of α-Fe_2O_3 consists in its poor kinetics, a common feature of all the materials presenting conversion reactions. Such kinetic limitations lead to a high overpotential (about 1 V), between the lithiation and delithiation processes, resulting in poor energy efficiency of the electrodes [8,9]. A suggested way to overcome the problem and improve the anode reactivity and cyclability resides in minimizing the material particle size [4,10]. Similar studies indicated that the synthetic route and the particle morphology also play a critical role in the electrochemical activity of such an anode material [11,12].

Mesoporous silicas, first developed in the early 1990s, are characterized by a tuneable porous structure which can be easily controlled by slightly modifying the synthesis conditions [13-16]. Hence, the advantage of using mesoporous silicas as hard templates lies in the possibility of having an indirect control over the structural-morphological parameters of its replica. To this purpose, mesoporous SBA-15 synthesized at different temperature were considered. In fact, as highlighted by A. Galarneau *et al.* [17], the SBA-15 precursor mesophase evolves as a function of the synthesis temperature: SBA-15 obtained at high temperature (i.e., 130 °C) possesses a micro/mesoporous structure that interconnects the mesopores one to each other. By decreasing the synthesis temperature, these interconnections progressively decrease, until complete disappearance.

In this paper, we present the characteristics of a novel nanostructured alpha iron oxide (α-Fe_2O_3), which generally reacts through a conversion mechanism, and its electrochemical behaviour as anode for lithium ion cells. For the above discussed reasons, the different α-Fe_2O_3 here presented were prepared in the form of nanostructured powders by a simple impregnation process, using iron (III) nitrate as precursor and mesoporous SBA-15 silicas having different textural features as hard templates. By means of a nanocasting strategy [18-20], the preformed mesoporous materials acted as a cage into which the inorganic precursors could be incorporated. After heat treatment and subsequent removal of the silica template, the nanostructured replica could be easily obtained. The Fe_2O_3 nanoparticles obtained as replicas reflected the progressive lack of interconnections above discussed, resulting in different lithium cell anode materials with interesting and peculiar electrochemical performances.

2. EXPERIMENTAL

2.1. Synthesis

Mesoporous SBA-15 silica templates were synthesized following a variation of the procedure described by Zhao et al. [16]. In a typical synthesis, 1.0 g of Pluronic P123 triblock co-polymer (Aldrich, EO_{20}-PO_{70}-EO_{20}) was dissolved in a solution of 5.5 ml of HCl (Fluka, HCl 37 wt. %) and 32 g of doubly distilled water. Afterwards, 2.1 g of tetraethyl orthosilicate (Aldrich, TEOS) were added to the solution under continuous stirring at 40 °C. After 20 h of continuous stirring at 40 °C, the white gel solution was transferred into a Teflon reactor and statically heated for 24 h at 130, 100 or 60 °C, respectively, to obtain different porous structures of the silica templates [17]. After cooling down to ambient temperature, the solid white products were recovered by filtering, washed several times with doubly distilled water and dried. Finally, the as-prepared SBA-15 powders were calcined at 520 °C for 10 h under air flow, for the complete surfactant removal.

The nanostructured α-Fe_2O_3 replicas were obtained according to the procedure reported hereafter [21]: 1.5 g of $Fe(NO_3)_3$ $9H_2O$ (Aldrich, 98 %) were dissolved in 20 ml of ethanol, followed by addition of 1.0 g of the selected mesoporous silica. After stirring at ambient temperature, until complete solvent evaporation, a dry powder was obtained. It was then calcined at 600 °C for 6 h, under air flow. Successively, the calcined powder was treated three times with 2.0 M NaOH (Aldrich) to remove the silica template, then washed several times with doubly distilled water and dried.

Three different mesoporous α-Fe_2O_3 were synthesized by the hard templating method. We will herewith label RS-130 the replica obtained from the SBA-15 prepared at 130 °C, while RS-100 and RS-60 will label the α-Fe_2O_3 from the SBA-15 obtained at 100 °C and 60 °C, respectively.

2.2. Structural-morphological characterization

The X-ray diffraction profiles of the samples were obtained using a Philips Xpert MPD powder diffractometer, equipped with Cu Kα radiation (V = 40 kV, i = 30 mA) and a curved graphite secondary monochromator. The diffraction profiles were collected in the 2θ range between 0.5° and 4° for the low diffraction angles patterns and between 20° and 70° for the high diffraction angles patterns, both with an acquisition step of 0.02° and a time per step of 10 s.

Specific surface areas (SSA) were determined using the Brunauer, Emmet, Teller (BET) method on an ASAP 2010 Micromeritics instrument. Prior to adsorption, approximately 50.0 mg of solid were placed in the cell and evacuated at 300 °C for 3 hours under high vacuum. The pore diameter distribution was evaluated by the Barrett-Joyner-Halenda (BJH) method, with the corrected form of the Kelvin equation, from the desorption branches of the isotherms.

The samples have also been submitted to a high-resolution transmission electron microscope (HRTEM) investigation for the morphological characterization, using a JEOL 2010 microscope with an accelerating voltage of 200 kV.

2.3. Electrochemical characterisation

The electrodes (geometrical area 0.785 cm^2, about 2 mg of weight) were prepared as a thin film over a copper foil current collector. A N-methyl-2-pyrrolidone (NMP, Aldrich) slurry of the as-prepared α-Fe_2O_3 mixed with acetylene black (Shawinigan Black AB50, Chevron Corp., USA) as electronic conductor and poly-(vinylidenefluoride) as binder (PVdF, Solvay Solef-6020), in the weight ratio of 70:20:10, was deposited over the current collector using a standard “doctor blade” technique.

Polypropylene three-electrode T-cells were employed to evaluate the electrochemical performance of the different samples. In a typical test, the cell was assembled as follows: the working electrode has the composition above described, a 1.0 M lithium hexafluorophosphate ($LiPF_6$, Aldrich) in a 1:1 w/w % mixture of ethylene carbonate (EC, Fluka) and diethyl carbonate (DEC, Aldrich) electrolyte solution soaked on a Whatman® GF/A separator and a lithium foil (high purity lithium foils, Chemetall Foote corporation) as the counter electrode. An additional lithium foil, acting as the reference electrode, was placed at the third opening of T-cell when cyclic voltammetry tests were carried out.

Galvanostatic discharge/charge cycling and cyclic voltammetry were performed at ambient temperature using an Arbin Instrument Battery Testing System model BT-2000. During cyclic voltammetry the electrode potential was scanned between 0.1 and 3.0 V vs. Li^+/Li at 0.100 mV sec^{-1}. The scan started from the cell open circuit potential (OCV) towards the reduction branch of the potential scan. The galvanostatic discharge/charge cycles were carried out at cut off voltages of 0.1 and 3.0 V vs. Li^+/Li, at C/10 current rate. In the tests, discharge refers to the lithiation process, while charge refers to the delithiation. All the measurements were performed at ambient temperature.

3. RESULTS AND DISCUSSION

3.1. Structural and morphological results

A complete structural analysis of the different mesoporous SBA-15 silica templates was carried out before the impregnation process.

The small-angle (2θ = 0.5 – 4°) X-Ray Powder Diffraction (XRPD) patterns of the different SBA-15 silica templates synthesized at 130, 100 and 60 °C are shown in Fig. 1.

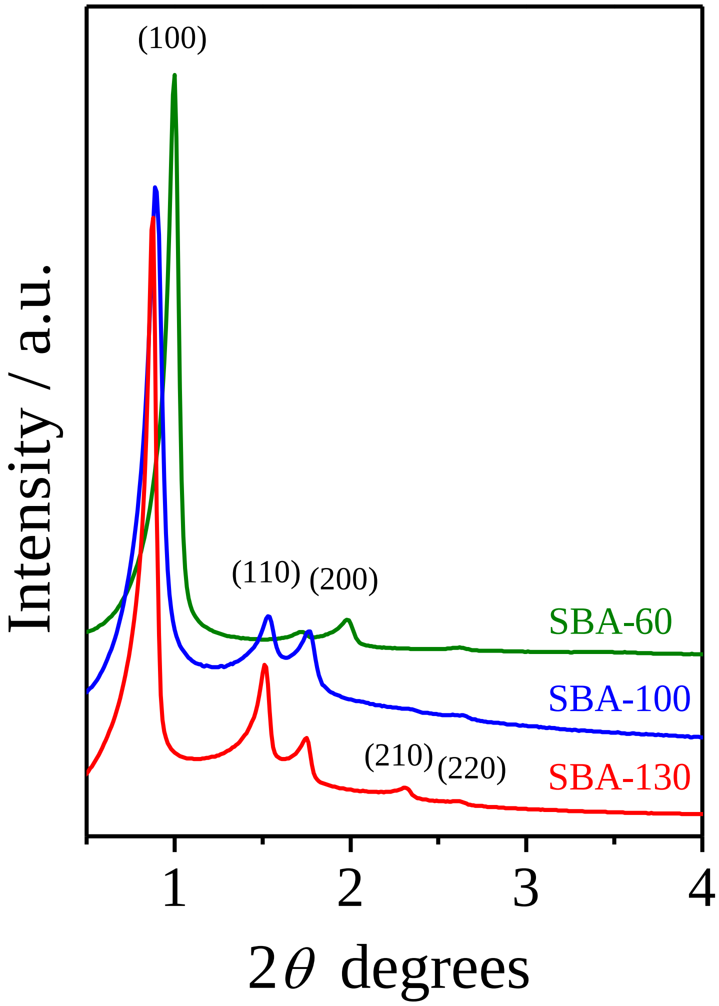

Figure 1. Low angle X-ray powder diffraction patterns (2θ = 0.5°–4°) of the SBA-15 samples, synthesized at different temperature, that is 130 (red line), 100 (blue line) and 60 °C (green line).

The XRPD pattern of SBA-130, synthesized at 130 °C (red line in Fig. 1), showed three well-resolved peaks centred at 2θ = 0.88, 1.51 and 1.75, respectively, indexed as (100), (110) and (200) reflections in the *p*6*mm* hexagonal symmetry. Two additional weak peaks in the 2θ range between 2.0° and 3.0°, corresponding to (210) and (220) scattering reflections, indicated that the synthesized SBA-15 possessed a high degree of hexagonal mesoscopic organization [22]. The (100), (110) and (200) reflections were also identified for the other two SBA-15, but in these cases the (110) and (200) reflections were less intense, most likely indicating silica structures with thicker walls or lower structural organization [17]. The decrease in the synthesis temperature affects the textural properties of the SBA-15, particularly below 100 °C. Actually, when compared to the other two samples, SBA-60 revealed a noticeable framework shrinkage which was deduced from the shift of the main reflections to higher 2θ values.

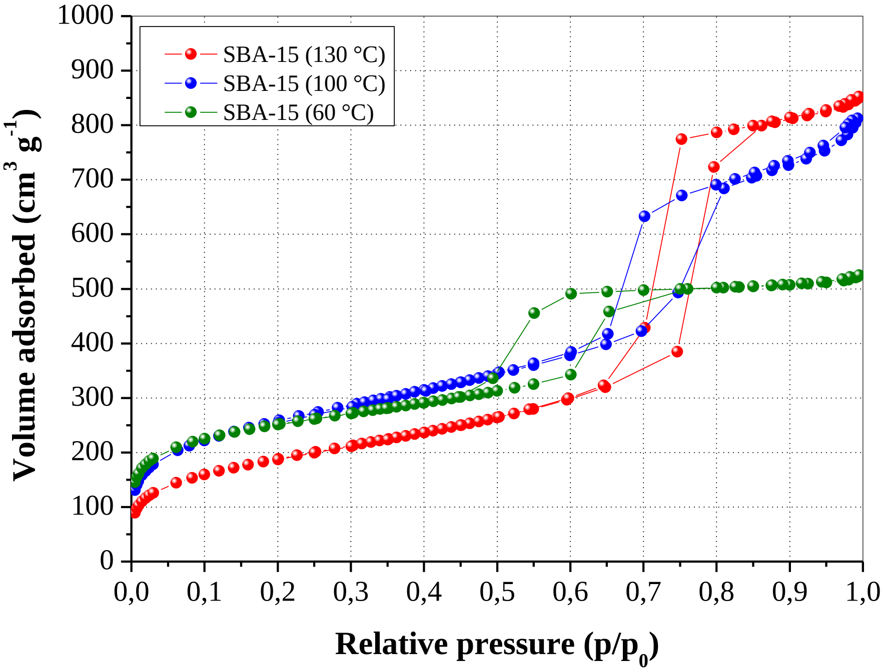

Figure 2. Nitrogen adsorption/desorption isotherms at 77 K of the SBA-15 hard templates, synthesized at different temperature.

Nitrogen adsorption/desorption isotherms at 77 K were carried out to study the textural properties of the silica templates and the changes induced by modification of the synthesis conditions. The isotherms for the synthesized silicas, depicted in Fig. 2, were similar to those reported in the literature [17]. Typical type-IV isotherms were obtained, as expected for such mesoporous materials according to IUPAC classification. For all the samples, three regions of the adsorption isotherms could be observed: a monolayer multilayer adsorption, a capillary condensation, and a multilayer adsorption on the outer particles surface. Overall, the isotherms presented similar features, with a sharp hysteresis loop corresponding to the filling of the mesopores. The relative pressure of pore filling increased with increasing the SBA-15 synthesis temperature, because of the progressive shrinkage of the silica walls. The observed trend resulted very similar to what is reported in the literature [17]. Table 1 summarizes the porous properties of the synthesized materials determined by BET and BJH methods, both obtained from the desorption branches of the isotherms.

Table 1. List of the synthesized mesoporous silica SBA-15 hard templates along with their porous properties.

Sample	Synthesis temperature (°C)	Specific surface area (m^2 g^{-1})	Pore diameter (nm)
SBA-130	130	655	7.5
SBA-100	100	868	6.5
SBA-60	60	875	4.3

Table 2. List of the synthesized nanostructured α-Fe_2O_3 samples along with their specific surface area (SSA, $m^2\ g^{-1}$) values.

Sample	Specific surface area ($m^2\ g^{-1}$)
RS-130	105
RS-100	90
RS-60	75

Table 2 lists the SSA values for the corresponding Fe_2O_3 samples: they are characterised by a very high specific surface area, with values ranging between 75 and 105 $m^2\ g^{-1}$. The drastic decrease in SSA moving from the template to its replica was expected, considering that the density for hematite is approximately twice that of silica.

The small-angle ($2\theta = 0.5 - 4°$) X-Ray Powder Diffraction (XRPD) patterns of the different Fe_2O_3 replicas are shown in Fig. 3a. Decreasing the synthesis temperature of the hard template, a loss of organisation was evident. Indeed, the sample RS-130 was ordered and its pattern showed two peaks characteristic of short-range ordering in mesoporous solids. By contrast, ordering highly reduced already for sample RS-100, and, moreover, only a broad shoulder was observed for sample RS-60.

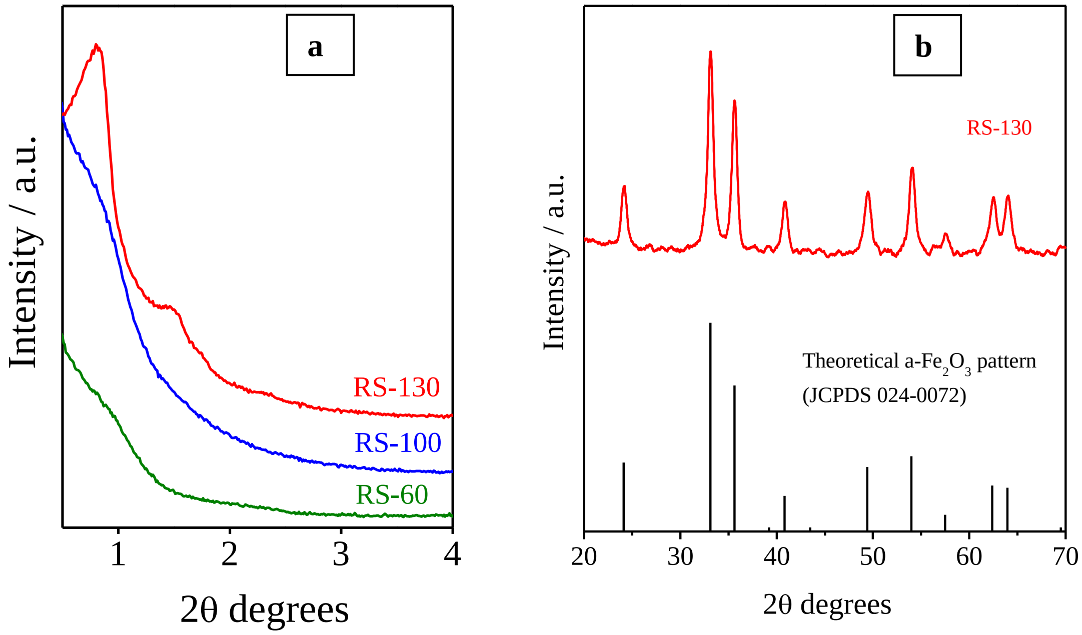

Figure 3. X-ray powder diffraction patterns of the three hematite samples. (A) Low angles diffraction patterns, $0.5° < 2\theta < 4°$, (B) wide angles diffraction pattern, $10° < 2\theta < 70°$, of sample RS-130 along with the corresponding α-Fe_2O_3 reference pattern.

The XRPD pattern at higher angles (2*θ* = 20 – 70°) of sample RS-130 is shown in Fig. 3b. It is representative for all the α-Fe_2O_3 materials prepared, as similar diffraction profiles were collected both for RS-100 and RS-60. The pattern was consistently indexed to the rhombohedral crystalline phase of hematite, α-Fe_2O_3, having the R-3c space group (JCPDS Card No. 024-0072). Additional contaminant crystalline phases were not detected, revealing the high purity degree of the synthesized material.

The nanostructured Fe_2O_3 materials were subjected to transmission electron microscopy (TEM) for morphological analysis. Representative high-resolution transmission electron microscopy (HR-TEM) images of the different α-Fe_2O_3 materials, taken with the beam parallel to the pore direction, are reported in Fig. 4-6, which confirm the successful replica of well crystallised Fe_2O_3 in SBA-15.

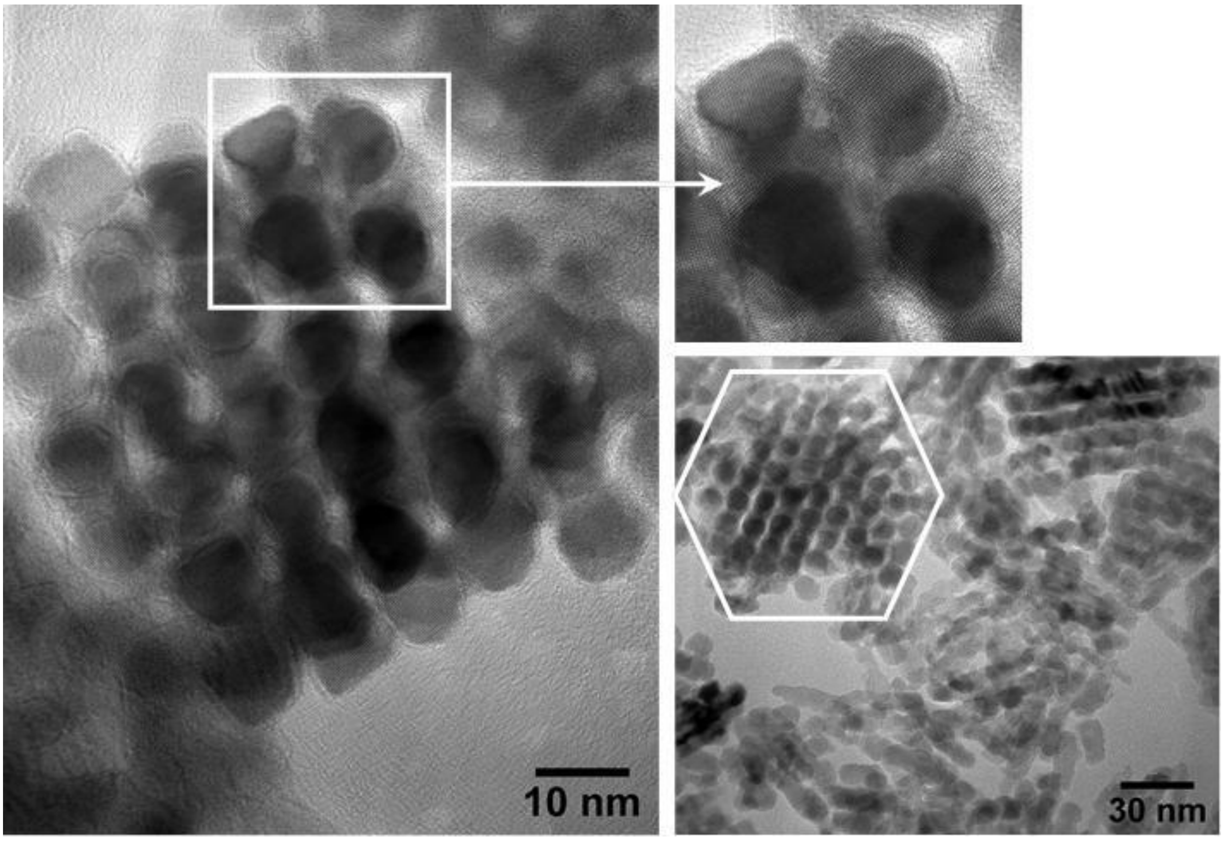

Figure 4. HR-TEM micrographs at different magnification of sample RS-130, obtained using SBA-15 hard template synthesized at 130 °C.

From the micrographs of sample RS-130 reported in Fig. 4, only nanoparticles, well-ordered and uniform in shape and size and arranged in a regular hexagonal structure were observed. Due to the presence of pores connecting the channels in the SBA-130 template, the resulting Fe_2O_3 nanoparticles were linked to each other. Thus, though the average particle diameter was about 10 nm, connections among particles generated aggregates larger than 100 nm. Conversely, TEM micrographs of sample RS-100 and RS-60, (Fig. 5 and Fig. 6, respectively), clearly showed a loss of hexagonal arrangement, as already evidenced by XRPD measurements.

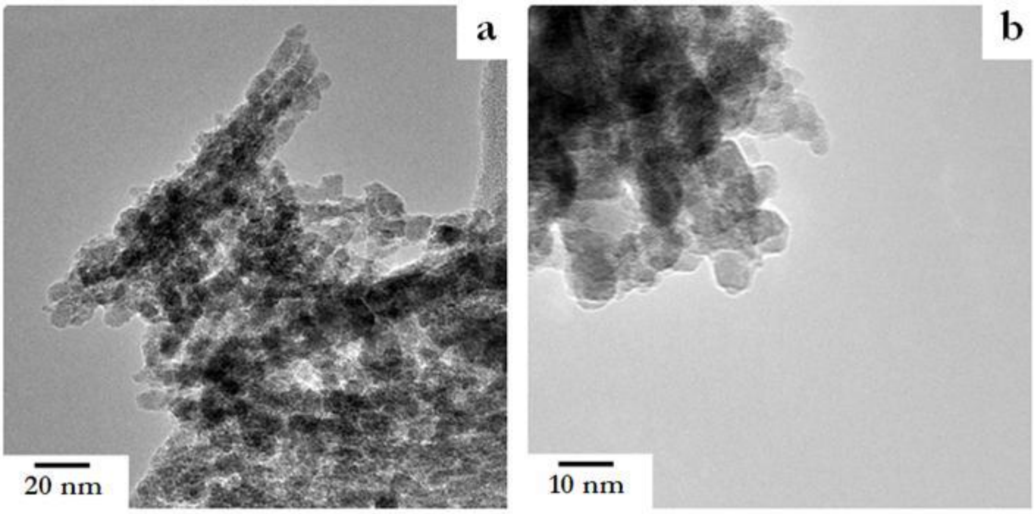

Figure 5. HR-TEM micrographs at different magnification of sample RS-100, obtained using SBA-15 hard template synthesized at 100 °C.

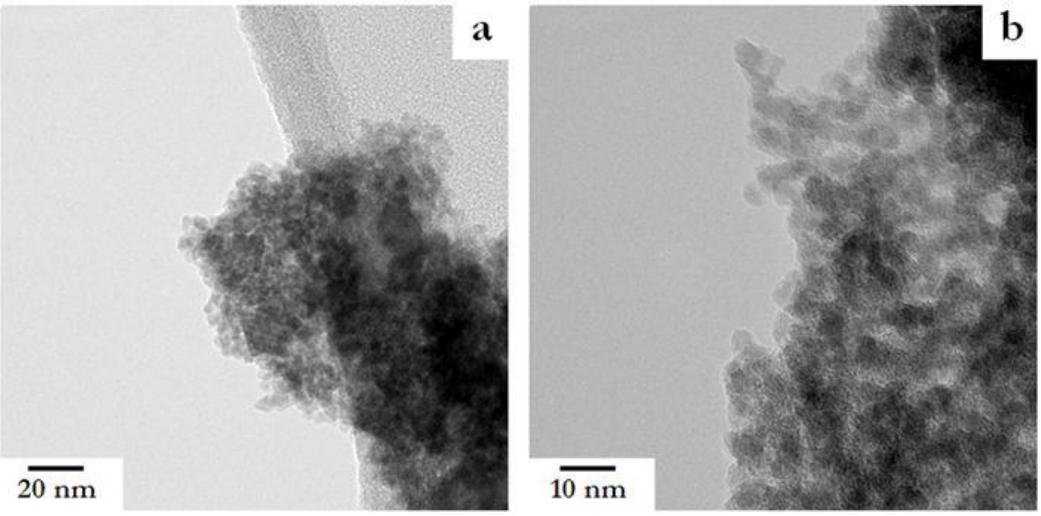

Figure 6. HR-TEM micrographs at different magnification of sample RS-60, obtained using SBA-15 hard template synthesized at 60 °C.

Sample RS-100 showed a decreased hexagonal order with respect to sample RS-130, nevertheless elongated structures were still present, due to the nucleation and growth of Fe_2O_3 particles inside the channels of the silica template, clearly visible in Fig. 5a. As expected, these features were not observed in the case of sample RS-60. In fact, by decreasing the synthesis temperature to 60 °C, the porosity among the template channels was greatly decreased and, correspondingly, the RS-60 nanoparticles were more fairly interconnected, resulting in lower aggregation. The average sizes of the nanoparticles were found to be also smaller than in sample RS-130, typically 8 nm for sample RS-100 and 4 nm for sample RS-60, due to the smaller pore sizes of the corresponding template obtained at lower synthesis temperatures.

3.2 Electrochemical results

Cyclic voltammetry (CV) is a basic instrumental method which is used to reveal the electrochemical mechanism of the reduction/oxidation reactions. Typical cyclic voltammograms recorded at ambient temperature for the three α-Fe_2O_3 electrodes between 0.1 and 3.0 V vs. Li^+/Li measured at a scan rate of 0.1 mV s^{-1} are shown in Fig. 7a (only selected cycles are shown for clarity purpose). All the samples showed substantially similar CV profiles: minor differences were observed only in the cathodic branch for sample RS-130. A comparison of these CV results indicates that qualitatively the trend was consistent with data reported in the literature [23-27], and the minor differences existing can be ascribed to the different nanostructures of the various samples which nontrivially influence the electrochemical behaviour of these materials [10,24,28,29]. Considering the difference in the reduction and oxidation peaks position and morphology, we can assume a reaction process which, during different phases, progressively leads to the formation of Li_2O along with the iron reduction. The complete reaction can be schematized as follows:

$$Fe_2O_3 + 6Li^+ + 6e^- \leftrightarrow 2Fe + 3Li_2O \tag{2}$$

After the first cycle (not shown here), the oxidation/reduction peaks resulted almost unchanged during CV for all the tested samples indicating the reversibility of the electrochemical reaction; a comparison with the results reported in literature [24-27] suggested that the prepared nanostructured Fe_2O_3 can act as conversion anode materials.

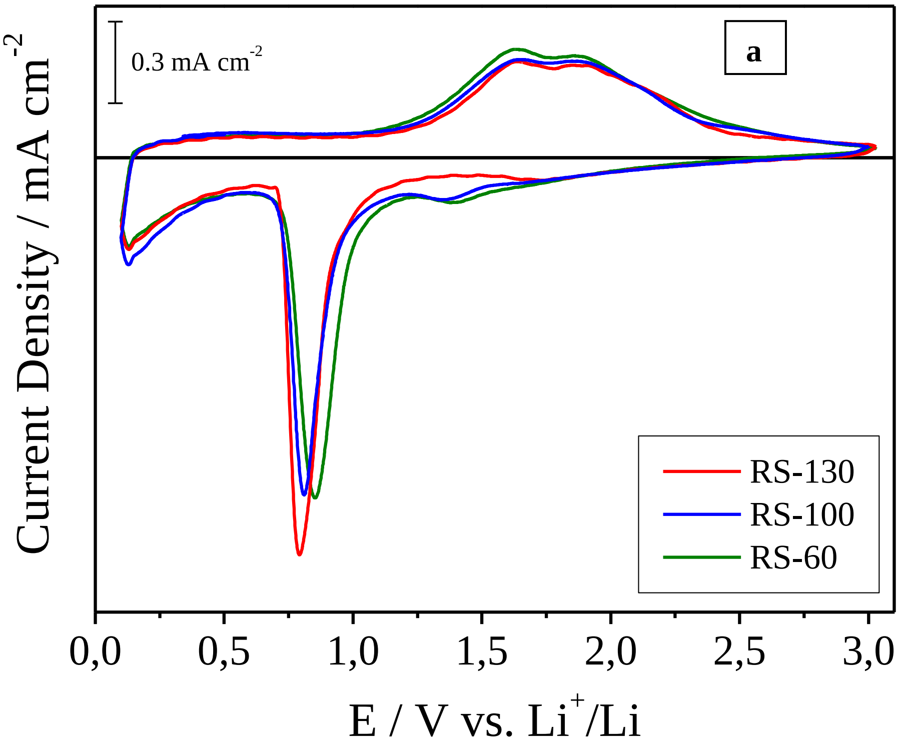

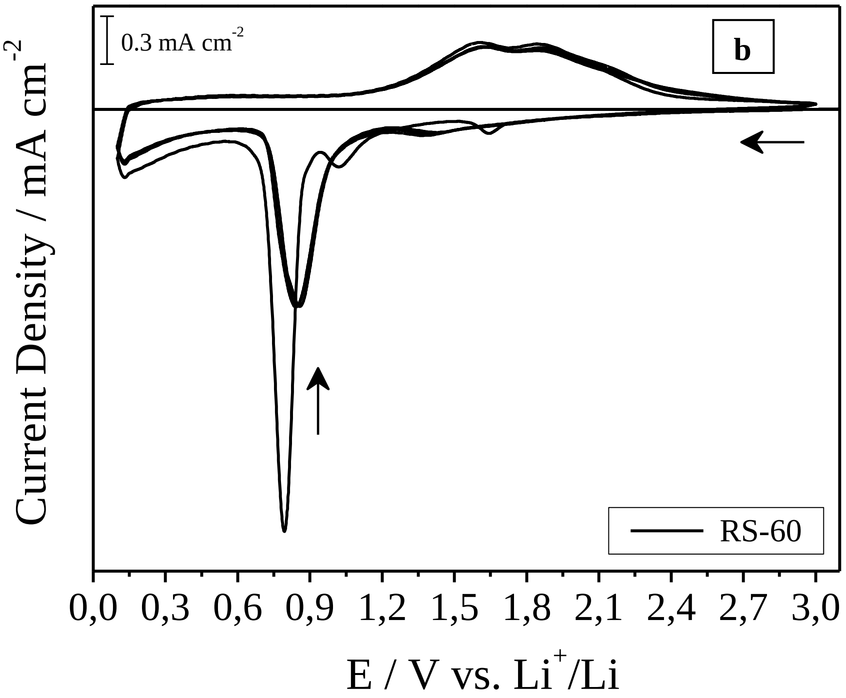

Figure 7. Cyclic voltammetries of the three hematite samples. Scan rate = 0.1 mV s^{-1} and potential range = 0.1–3.0 V vs. Li^+/Li. (A) Typical 3rd voltammetric cycle for RS-130 (red line), RS-100 (blue line) and RS-60 (green line) samples; (B) Cyclic voltammetry (cycles from 1 to 5) of sample RS-60.

In order to accurately investigate the different redox processes occurring, the initial five cyclic voltammograms of RS-60, representative for all the samples prepared, are shown in Fig. 7b. A substantial difference between the first and the following cycles, especially for the main cathodic process, clearly revealed the formation of irreversible products, which also include the formation of the SEI (Solid Electrolyte Interphase) layer on the iron oxide nanoparticles surface. During the first scan, which started from the cell open circuit potential (ca. 3.04 V vs. Li^+/Li) towards the reduction branch of the potential, three cathodic peaks centred at about 1.65, 1.02 and 0.79 V vs. Li^+/Li were observed. According to the mechanism proposed in the literature [10,23,24], the first two peaks can be associated to the intercalation of Li^+ ions into the host crystal structure of the nanostructured α-Fe_2O_3, which leads to the coexistence of two lithium-intercalated $Li_2(Fe_2O_3)$ phases (i.e., cubic and hexagonal) corresponding to a small amount of lithium storage. These two peaks almost disappeared during the following cycles (in fact, only a weak peak located in the range of 1.35–1.45 V vs. Li^+/Li remained) indicating the poor reversibility of the associated processes. The high intensity spiky peak centred at about 0.79 V vs. Li^+/Li was likely attributed to the reduction of Fe^{3+} to Fe^0 in the cathodic process along with the conversion reaction of lithium ions to form Li_2O including, during the first reduction, electrolyte decomposition to form the SEI layer. The formation of the SEI layer at such potential values, resulting in the evolution of an organic layer that is deposited onto the surface of the particles, is consistent with many articles published in the literature [10,23,24], confirmed also by TEM observations on similar systems. In the following scan towards the oxidation branch of the potential, only two main overlapping broad peaks were recorded in the range of 1.5–1.9 V vs. Li^+/Li, ascribable to the reversible oxidation process of Fe^0 to Fe^{3+} in two steps (i.e., $Fe^0 \rightarrow Fe^{2+}$ at about 1.6 V and, then, $Fe^{2+} \rightarrow Fe^{3+}$ at about 1.85 V vs. Li^+/Li).

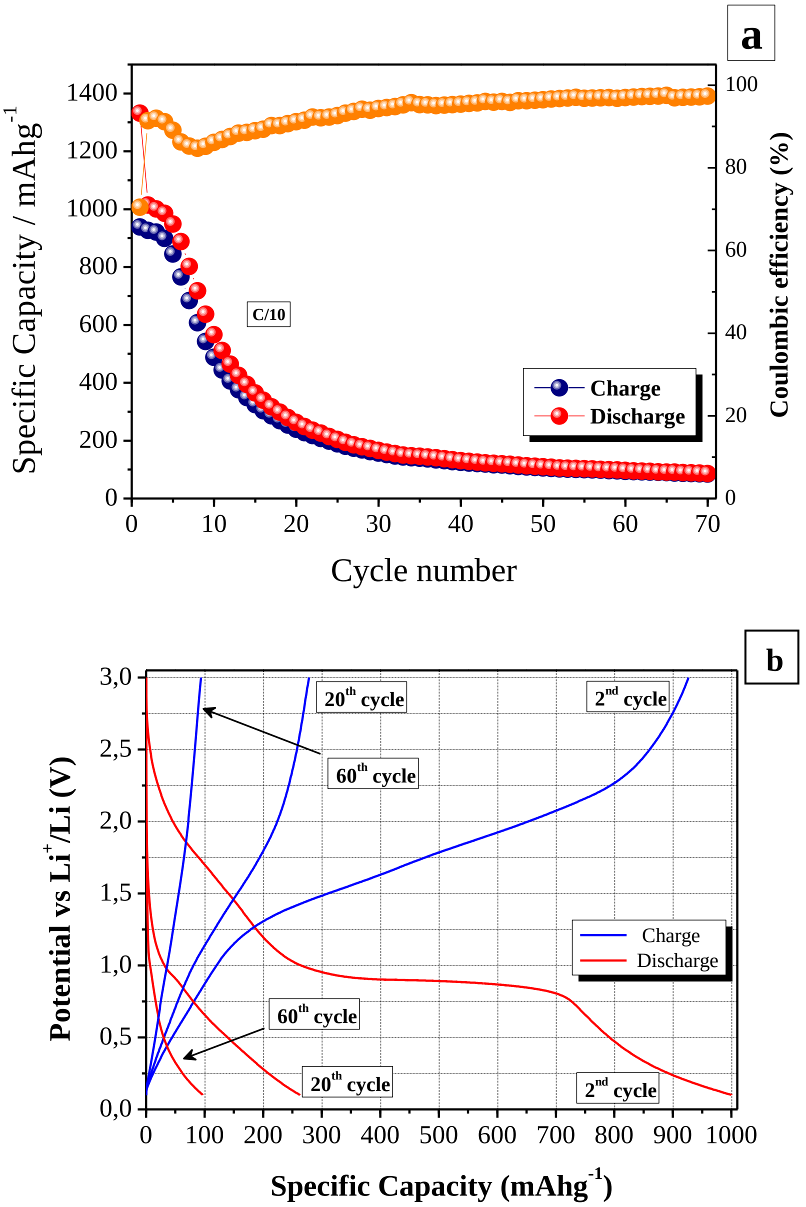

Figure 8. Constant current discharge/charge cycling test at ambient temperature and at the current regime of C/10 of RS-130 Fe_2O_3 sample: a) specific discharge/charge capacities and Coulombic efficiency with cycling and b) voltage profiles after different cycles.

During the second anodic scan, the profile differs considerably from the first, suggesting drastic lithium-driven structural and/or textural modifications. The first two cathodic peaks almost disappeared; the strong peak was shifted to higher potential values and both the peak intensity and the integrated area were reduced, indicating capacity loss due to the irreversible processes previously discussed. The subsequent voltammetric cycles, both in the cathodic and anodic sweep, were increasingly similar, the CV peaks overlapping well, thus being almost stable during cycling in intensity and integrated area. According to the discussed CV results, the electrochemical iron oxidation/reduction processes were found to be reversible, and this can be ascribed to the high surface area and nanostructuration which shortens the diffusion path for the Li^+ ions thus favouring the reversibility.

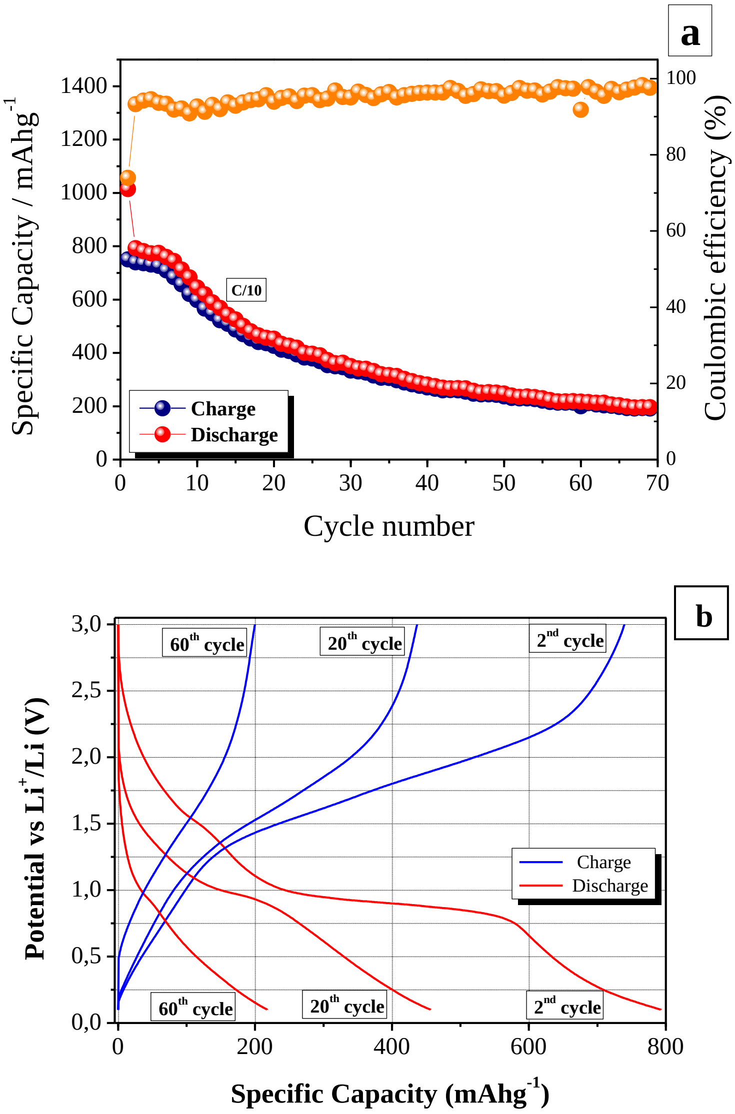

Figure 9. Constant current discharge/charge cycling test at ambient temperature and at the current regime of C/10 of RS-100 Fe_2O_3 sample: a) specific discharge/charge capacities and Coulombic efficiency with cycling and b) voltage profiles after different cycles.

We next studied the electrochemical properties of the materials in lithium cells by cyclic galvanostatic discharge/charge cycling. Ambient temperature discharge/charge galvanostatic cycling for the three nanostructured hematite samples at C/10 in the potential range between 0.1 and 3.0 V vs. Li^+/Li is shown in Figs. 8, 9 and 10: specific capacity versus cycle number in plot a) and potential profiles versus time in plot b).

The specific capacity of RS-130 reached 1331 mAh g^{-1} at the end of the first full discharge process, values slightly lower were obtained for RS-100 and RS-60, namely 1014 mAh g^{-1} and 1118 mAh g^{-1}, at the same discharge rate. The extra capacity beyond the theoretical, related to the decomposition of the electrolyte and SEI formation [23,31], led to a relatively low irreversible capacity loss of about 29.0 % for all the tested samples between the first and second discharge cycles; similar values were recently reported in the literature by Wang et al. [32]. Observing the potential profiles, a clear plateau can be identified at about 0.8 V vs. Li^+/Li in the early discharge cycles (plots b of Figs. 8, 9 and 10), in complete agreement with the CV measurements.

This reaction gives rise to the major contribution to the Li storage capability of the synthesized materials [32] and explains the high values of the discharge capacity in the early cycles. The opposite reaction, involving the decomposition of the Li_2O-matrix and the formation of Fe^{3+}, evolves as a S-type shaped curve centred at higher potential values (about 1.5 V vs. Li^+/Li), with no discernable plateau.

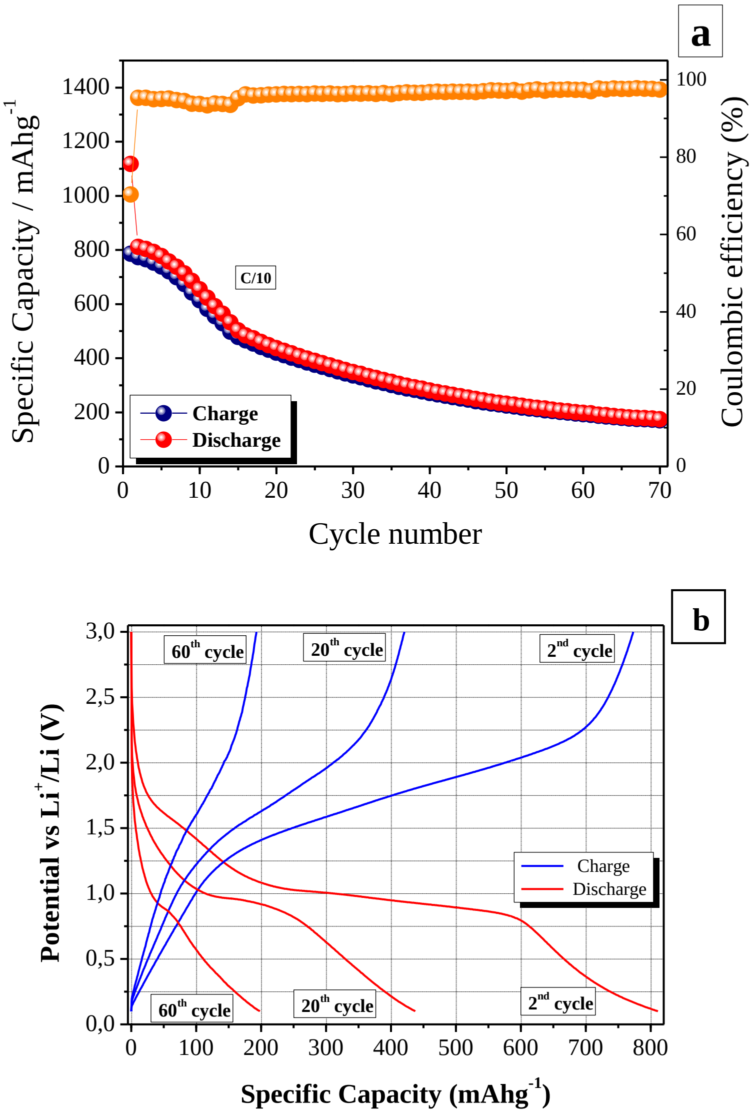

Figure 10. Constant current discharge/charge cycling test at ambient temperature and at the current regime of C/10 of RS-60 Fe_2O_3 sample: a) specific discharge/charge capacities and Coulombic efficiency with cycling and b) voltage profiles after different cycles.

From the 2nd cycle onwards the electrodes showed a good initial capacity retention (see Table 3), comparable with most of the results reported in the literature [25-27,33-35]. In order to emphasize the results obtained, it is important to note that, in our case, the hematite nanoparticles were bare, not carbon coated, and 20 wt. % of conducting carbon additive was added during the preparation of the electrodes, while in general the quantity of carbon used during the preparation of the electrodes is definitely larger, reaching in some cases even the 50 wt. % of the total electrode weight [25, 30,36].

Table 3. Summary of discharge/charge capacity values after different number of galvanostatic cycles down to full discharge and the correspondent capacity retention for the RS-130, RS-100 and RS-60 hematite samples.

Cycle number	RS-130		RS-100		RS-60	
	Charge capacity (mAh g^{-1})	Capacity retention (%)	Charge capacity (mAh g^{-1})	Capacity retention (%)	Charge capacity (mAh g^{-1})	Capacity retention (%)
1	938		750		786	
5	845	90	726	97	739	94
10	488	52	598	80	614	78
15	325	34	488	65	479	61
20	227	24	426	57	421	54
30	156	17	333	44	336	43
40	125	13	271	36	271	34
50	105	11	236	31	225	29
60	94	10	200	27	193	27
70	82	8	191	25	170	24

After 10 charge/discharge cycles, the electrodes were able to deliver about 80 % of the initial reversible specific capacity; moreover, after 30 cycles, the capacity retention of the samples RS-100 and RS-60 was still 44 % and 43 %, respectively. This feature was less noticeable for RS-130 (Fig. 8), meaning that the lower structuration of RS-100 and RS-60 materials (Fig. 9,10) mitigates the degradation problems occurring during cycling. The explanation in the observed decrement in the reversible capacity upon prolonged cycling can be related to the repeated expansion/shrinkage of the structure caused by the conversion reaction that leads to strong mechanical stresses affecting the electrode integrity (e.g., cracks and/or detachment from the substrate, etc.), causing also the increase in the electrode resistance with cycling as active iron metal may be progressively isolated by the non-conducting materials such as Li_2O and organic passive film [23]. As a consequence, these problems definitely limit the long-term electrochemical performance of the electrode. In this respect, the structure of RS-130, with nanoparticles bonded together in highly ordered aggregated clusters, is probably the cause of the faster electrode degradation. Conversely, the long-term cycling performances of RS-100 and RS-60 were noticeably improved and, after 70 cycles, the electrodes were still able to deliver about 25 % of the initial reversible specific capacity. The improved capacity could be attributed to the structure of the materials possessing smaller grain sizes (see Fig. 5-6) and having lower long range organisation, which, consequently, suffer less from the structural degradation and better retain the contact among the particles, resulting in higher long-term conductivity retention and stability.

The thorough analysis of the first discharge (lithium uptake) curves down to full reduction (low potential cut-off voltage at 0.100 V vs. Li^+/Li) can provide some useful information regarding the electrochemical processes.

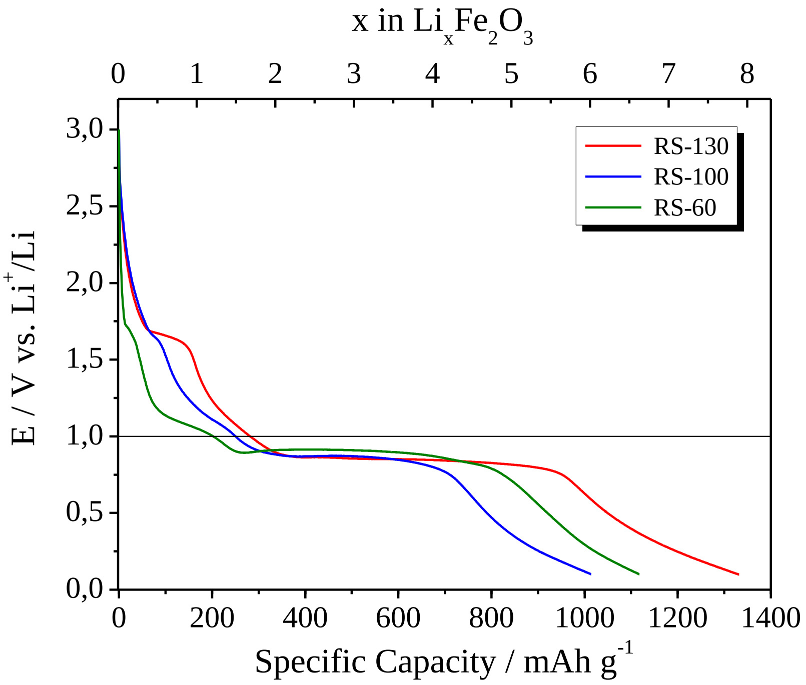

Figure 11. First discharge profiles of the three α-Fe_2O_3 electrodes. Voltage range = 0.1 – 3.0 V vs. Li^+/Li, C/10 current regime. The line at 1.0 V vs. Li^+/Li separates the high and low potential regions.

Fig. 11 shows the ambient temperature first discharge curves collected at C/10 current rate for the three hematite samples prepared. The profiles are strictly related to the curves obtained by cyclic voltammetry during the first reduction, indicating the complementary nature of the galvanostatic and CV data. On the basis of the complete reduction of Fe^{3+} to Fe^0, as from eq. (2), the theoretical capacity of Fe_2O_3 was estimated to be 1007 mAh g^{-1}, corresponding to the maximum exchange of 6 Li moles per formula unit. From the analysis of the current profiles, high lithium uptake was demonstrated for all the curves as above 6 Li per α-Fe_2O_3: more precisely, 7.95, 6.05, 6.65 Li per RS-130, RS-100 and RS-60 can be reacted, respectively, corresponding to 1331, 1014 and 1118 mAh g^{-1}. As previously discussed, the excess in specific capacity was likely ascribable to the SEI layer formation. In all the curves we can easily distinguish two regions (i.e., above and below 1.0 V vs. Li^+/Li) in which two different mechanisms occur. In the potential region below 1.0 V vs. Li^+/Li, the profiles were similar, showing a long plateau at about 0.8 V which is due to the formation of metallic iron along with the conversion reaction of lithium ions to form Li_2O and the well-known decomposition of the electrolyte to form the SEI layer which occurs at low-potential, below 0.8 V vs. Li^+/Li [25,30]. Interestingly, the profiles were noticeably different in the high potential region above 1.0 V vs. Li^+/Li. In particular, RS-130 showed a neat potential plateau at about 1.65 V, which is attributed to the intercalation of about 1.75 mol of Li^+ ions inside the crystal structure of the nanostructured α-Fe_2O_3, corresponding to a capacity of about 290 mAh g^{-1}. On the contrary, samples RS-100 and RS-60 showed a lower consumption of lithium ions until 1.0 V, that is about 1.50 and 1.25 (i.e., 249 and 201 mAh g^{-1}, respectively); the plateaus were clearly less pronounced and progressively shifted to lower potential values. This is in agreement with the first reports by Larcher et al. [10], thus, as the three materials are chemically and structurally alike, the morphological discrepancies such as the particle size and specific surface area are responsible for the lithium intercalation performance in the crystal structure of α-Fe_2O_3 before the low-potential structural transformation.

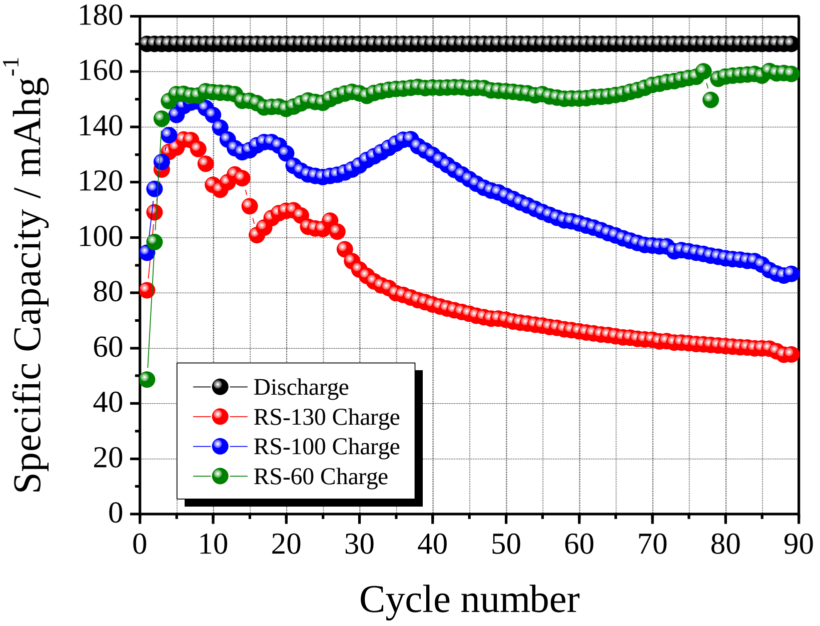

Figure 12. Constant current discharge/charge cycling test at ambient temperature and at the current regime of C/10 of the three hematite samples, under a 170 mAh g^{-1} capacity limit upon discharge.

Taking into account that the use of negative electrodes having high working potentials, despite a lower overall energy density, can lead to the assembly of intrinsically safer batteries, we finally investigated the galvanostatic discharge/charge behaviour of the three hematite-based electrodes at ambient temperature with a current regime of C/10 under a 170 mAh g^{-1} capacity limit upon discharge, that is the capacity corresponding to the theoretical intercalation of 1 Li^+ in the Fe_2O_3 structure. Aim of this test was to minimize the expansion/shrinkage of the structure avoiding the complete lithiation/delithiation processes and conversion reaction. Also in this case the correlation between electrochemical performances, particularly the cycling stability, with the textural features of the Fe_2O_3

samples was well evident. The results obtained from the constant current galvanostatic cycling tests (specific capacity versus cycle number) are shown in Fig. 12. A sharp decrease in the delivered specific charge capacity was evident for sample RS-130 and RS-100, starting from the 26th and the 37th cycle, respectively. This behaviour is a clear indication of degradation occurring upon cycling, as previously evidenced. On the contrary, noticeable results were obtained in the case of sample RS-60, able to deliver a constant and stable capacity, near the theoretical value upon charge, for 90 cycles without evidences of degradation, most likely ascribable to its structural-morphological characteristics.

To the best of our knowledge, such an appreciable result has not been reported so far [10,30]. Thus, when considering Li-based cells conceived for intrinsically safer applications, electrode materials like RS-60, having lower long-range organisation and smaller nanosized grains, could be the electrodes of choice as they can guarantee better capacity retention upon prolonged cycling.

4. CONCLUSIONS

In summary, we prepared crystalline hematite nanoparticles with easily tunable morphologies/textures and high surface area by nanocasting strategy which includes the use of silica as hard template followed by wetness impregnation and heat treatment. Exploiting the characteristics of the silica framework, a careful control over the size and shape of the α-Fe_2O_3 particles was achieved, through a very simple and fast synthesis route. The electrochemical behaviour of the samples was tested into lab-scale lithium cells with liquid electrolyte. Our study indicated that, depending on their textural/morphological characteristics, the materials showed different electrochemical responses. The gradual loss of specific capacity after several galvanostatic cycles down to full discharge was ascribed to the conversion reaction causing progressive electrode deterioration. Nevertheless, particularly when actions are taken to prevent this deterioration (e.g., reaction of only 1 Li^+ ion per Fe_2O_3 formula unit), electrodes like RS-60, having smaller particles size and lower long-range organisation, can retain specific capacities near the theoretical value and guarantee a very good capacity retention upon prolonged cycling.

Overall, our proposed method is novel and simple, with no critical parameters. It can provide a new, easy and low cost approach to fabricate nanostructured conversion electrodes having high working potential and, thus, interesting characteristics for the next generation of advanced safer Li-ion batteries. Preliminary results reported in the present paper are encouraging, but improvements are certainly necessary in particular for what concerns the long-term performance of the electrode upon prolonged cycling down to full discharge. Extensive experimental investigations on this subject are in progress to optimise the materials characteristics.

ACKNOWLEDGEMENTS
The authors would like to thank Dr. M. Daniel for the TEM and Dr. F. Bossolet for the XRD analysis of the samples.

References

1. P.G. Bruce, B. Scrosati, and J-M. Tarascon, *Angew. Chem. Int. Ed.*, 47 (2008) 2930
2. W.J. Zhang, *J. Power Sources*, 196 (2011) 13
3. G.K. Simon, and T. Goswami, *Metall. Mat. Trans.*, A 42A (2011) 231
4. J-M. Tarascon, and M. Armand, *Nature*, 414 (2001) 359
5. P. Poizot, S. Laruelle, S. Grugeon, L. Dupont, and J.-M. Tarascon, *Nature*, 407 (2000) 496
6. H. Li, Z. Wang, L. Chen, and X. Huang, *Adv. Mater.*, 21 (2009) 4593
7. J. Cabana, L. Monconduit, D. Larcher, and M.R. Palacín, *Adv. Mater.*, 22 (2010) E170
8. S. Mizutani, and Y. Kudo, United States Patent Application, 20 060 121 348 (2006)
9. I. Amadei, S. Panero, B. Scrosati, G. Cocco, and L. Schiffini, *J. Power Sources*, 143 (2005) 227
10. D. Larcher, C. Masquelier, D. Bonnin, Y. Chabre, V. Masson, J-B. Leriche, and J-M. Tarascon, *J. Electrochem. Soc.*, 150 (2003) A133
11. M.S. Whittingham, *Dalton Trans.*, (2008) 5424
12. P.G. Bruce, *Solid State Sci.*, 7 (2005) 1456
13. J.S. Beck, J.C. Vartuli, G.J. Kennedy, C.T. Kresge, W.J. Roth, and S.E. Schramm, *Chem. Mater.*, 6 (1994) 1816
14. Q. Huo, D.I. Margolese, and G.D. Stucky, *Chem. Mater.*, 8 (1996) 1147
15. D. Zhao, J. Feng, Q. Huo, N. Melosh, G.H. Fredrickson, B.F. Chmelka, and G.D. Stucky, *Science*, 279 (1998) 548
16. D. Zhao, J. Sun, Q. Li, and G.D. Stucky, *Chem. Mater.*, 12 (2000) 275
17. A. Galarneau, H. Cambon, F. Di Renzo, R. Ryoo, M. Choi, and F. Fajula, *New J. Chem.*, 27 (2003) 73
18. H. Yang, and D. Zhao, *J. Mater. Chem.*, 15 (2005) 1217
19. R. Ryoo, S.H. Joo, and S. Jun, *J. Phys. Chem. B*, 103 (1999) 7743
20. A.H. Lu, and F. Schüth, *Adv. Mater.*, 18 (2006) 1793
21. F. Jiao, A. Harrison, J.-C. Jumas, A. V. Chadwick, W. Kockelmann, and P.G. Bruce, *J. Am. Chem. Soc.*, 128 (2006) 5468
22. C. Gerbaldi, G. Meligrana, S. Bodoardo, A. Tuel, and N. Penazzi, *J. Power Sources*, 174 (2007) 501
23. M-S. Wu, Y-H. Ou, and Y-P. Lin, *J. Electrochem. Soc.*, 158 (2011) A231
24. M.V. Reddy, T. Yu, C.-H. Sow, Z.X. Shen, C.T. Lim, G.V. Subba Rao, and B.V.R. Chowdari, *Adv. Funct. Mater.*, 17 (2007) 2792
25. H. Liu, G. Wang, J. Park, J. Wang, H. Liu, and C. Zhang, *Electrochim. Acta*, 54 (2009) 1733
26. H. Liu, D. Wexler, and G. Wang, *J. All. Comp.*, 487 (2009) L24
27. H.S. Kim, Y. Piao, S.H. Kang, T. Hyeon, and Y.-E. Sung, *Electrochem. Comm.*, 12 (2010) 382
28. J. Morales, L. Sánchez, F. Martín, F. Berry, and X. Ren, *J. Electrochem. Soc.*, 152 (2005) A1748
29. J. Chen, L.L. Xu, W. Li, and X. Gou, *Adv. Mater.*, 17 (2005) 582
30. P. Tartaj, and J.M. Amarilla, *J. Power Sources*, 196 (2011) 2164
31. G. Wang, J. Park, J. Wang, H. Liu, and C. Zhang, *Electrochim. Acta*, 54 (2009) 1733
32. B. Wang, J.S. Chen, H.B. Wu, Z. Wang, and X.W. Lou, *J. Am. Chem. Soc.*, 133 (2011) 17146
33. M-S. Wu, Y-H. Ou, and Y-P. Lin, *Electrochim. Acta*, 55 (2010) 3240
34. S. Hariharan, K. Saravanan, and P. Balaya, *Electrochem. Sol. State Lett.*, 13 (2010) A132
35. L. Chun, X. Wu, X. Lou, and Y. Zhang, *Electrochim. Acta*, 55 (2010) 3089
36. M.F. Hassan, M.M. Rahman, Z.P. Guo, Z.X. Chen, and H.K. Liu, *Electrochim. Acta*, 55 (2010) 5006